Formation and Catalytic Performance of Supported Ni Nanoparticles via Self-Reduction of Hybrid NiAl-LDH/C Composites

Xu Xiang, Lu Bai, and Feng Li
State Key Laboratory of Chemical Resource Engineering, Beijing University of Chemical Technology, Beijing 100029, P.R. China

DOI 10.1002/aic.12189
Published online February 24, 2010 in Wiley Online Library (wileyonlinelibrary.com).

In the present work, hybrid NiAl-layered double hydroxide/carbon (LDH/C) composites with adjustable compositions were successfully assembled by crystallization of LDH in combination with carbonization of glucose under hydrothermal conditions, and further utilized as an integrated catalyst for the growth of carbon nanotubes (CNTs) in catalytic chemical vapor deposition (CCVD) of acetylene. The materials were characterized by X-ray diffraction, Fourier transform infrared, elemental analysis, thermogravimetric and differential thermal analysis, SEM, transmission electron microscopy, X-ray photoelectron spectra, and Raman spectroscopy. The results revealed that the supported Ni nanoparticles with the small crystallite size of about 10 nm could be obtained by in situ self-reduction of as-assembled hybrid LDH/C composites in the course of CCVD. The carbon in the hybrid structure as a reducing agent played a key role for the high dispersion of resulting Ni nanoparticles. Furthermore, the Ni nanoparticles obtained here exhibited excellent activity for catalytic growth of CNTs, which could be delicately tuned by varying the compositions of hybrid composites. © 2010 American Institute of Chemical Engineers *AIChE J,* 56: 2934–2945, 2010

Keywords: hybrid composite, layered double hydroxide, carbon, carbon nanotubes, catalysis

Introduction

Layered double hydroxides (LDHs, $[M^{2+}_{1-x}M^{3+}_{x}(OH)_2]^{x+}[A_{x/n}]^{n-}\cdot mH_2O$) belong to a family of anionic clay materials with $[Mg(OH)_2]$ brucite-like layered structure.[1] The divalent metal cations can be partially substituted by trivalent ones within the layers of LDHs to give a positively charged layer balanced by the intercalation of anions in the interlayer regions,[1–3] thus giving rise to uniform distribution and ordered prearrangement of metal cations in the layers. Owing to the tunable composition of metal cations in the layers and flexible exchangeability of interlayer anions, LDHs have a large number of potential applications in a variety of fields used as catalysts, adsorbents, additives in polymers, and precursors to functional materials.[4–9] Among various catalysis applications, a prevailing class of catalyst constitutes well-dispersed, catalytically active supported metal nanoparticles, which can be obtained by reducing calcined LDHs containing desired metals either in the form of metal cations on the layers or in the form of metal complexes in the interlayers.[10–12] This kind of structural transformation endows LDH materials with excellent capability in various metal-catalyzed reactions.[13–17]

It is known that there are three well-established synthesis techniques for carbon nanotubes (CNTs), that is, arc discharge, laser ablation, and catalytic chemical vapor deposition (CCVD).[18–20] Among them, CCVD technique shows the

Additional Supporting Information may be found in the online version of this article.

Correspondence concerning this article should be addressed to F. Li at lifeng_70@163.com.

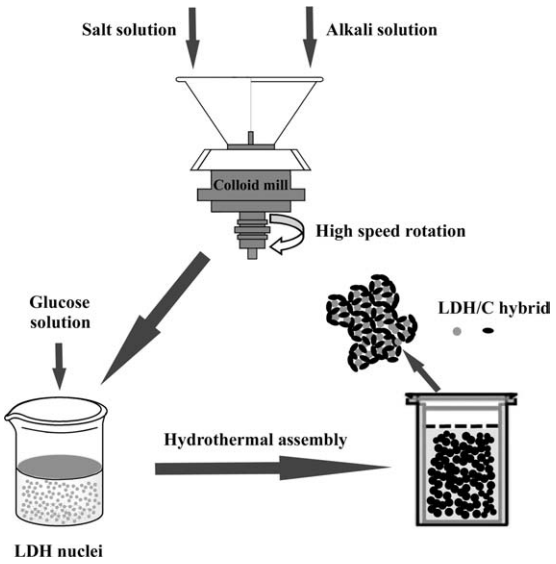

Scheme 1. Hydrothermal assembly of LDH/C nanocomposites.

greatest potential for economically feasible, large-scale synthesis based upon high yields and reproducibility. The formation of CNTs by CCVD routes occurs through the catalytic decomposition of a carbonaceous gas on nanometric metal particles, which are typically transition metals (iron, nickel, cobalt, and their alloys).[21–23] The most common way for obtaining metal nanoparticles is to load active component precursors or metal nanoparticles onto various supports with high-surface area to disperse and stabilize metallic particles, such as oxides or zeolites.[24–26] It is reported that the formation of large nanoparticle agglomerates of catalyst is necessary for scalable synthesis of CNTs in a fluidized-bed CCVD process providing optimal gas–solid mixing, heat and mass transfer.[22,27] To ensure good fluidization, alumina, silica, and zeolite are commonly used as catalyst supports because they are inert at high temperatures. Although the supported catalysts may be fragmented by the mechanical stress in the fluidized-bed reactor, the resulting subagglomerates of catalysts can expand into large agglomerates combined with CNTs formed in the CCVD process.[28] On the other side, the synthesis parameters for catalysts, such as compositions, loading amounts, and loading ways of catalysts have significant effects on the microstructures and the shapes of obtained carbon nanostructures.[29–31] Recently, the catalytic growth of carbon nanostructures has been achieved using LDH-derived catalysts via CCVD.[32–38] Our work has also verified that highly active cobalt-based supported nanoparticles capable of catalyzing the growth of CNTs could be produced by calcination of LDH precursor and subsequent reduction,[39,40] and found that the obtained CNTs have considerable yields and relatively thin diameters owing to high loadings and good dispersion of active species. When compared with other metal-supported catalysts, LDH materials as catalyst precursors have two advantages for growth of carbon nanostructures: (i) Active components with adjustable content can be uniformly integrated into the LDH structure, owing to the ordered prearrangement of divalent and trivalent cations at an atomic level in precursor; (ii) metal nanoparticles with tunable particle size can be formed by the reduction of calcined LDH materials in a controllable manner. However, in the earlier cases, the whole growth process of CNTs involved calcination of LDH precursors, reduction of calcined product under the reducing atmosphere (usually H_2), and catalytic growth of CNTs, which unambiguously increases the complexity of production and is of time- and energy-consuming.

In our previous work, we reported the formation of mesoporous-mixed metal oxides with high-surface area and narrow pore size distribution through two stages of assembly of hybrid NiAl-LDH/carbon composite and successive calcination.[41] The NiAl-LDH/carbon composite was formed by crystallization of NiAl-LDH and simultaneous carbonization of glucose under hydrothermal conditions, and then mesopores were produced due to the removal of carbon template through calcining the composite in air. Based on the idea that the carbon in the composite may be expected as a reducing agent, probably leading to in situ reduction of metal anions upon heating in the absence of H_2, in this contribution, we have extended to the controlled formation of supported Ni nanoparticles during the CCVD by fabricating hybrid NiAl-LDH/C composite, in our prospects to make hybrid composite an alternative candidate for active supported Ni nanoparticles with high metal loading to effectively catalyze the growth of CNTs. To our best knowledge, detailed studies of supported Ni nanoparticles dispersed and stabilized into alumina and carbon support matrix based on in situ self-reduction of hybrid composites for the growth of CNTs have not been reported before. Moreover, this strategy provides a simplified production of CNTs at low cost. It is expected that similar to other supported catalysts easy to fluidize, the as-synthesized supported Ni catalyst should be suitable in a fluidized-bed reactor for practical production of CNTs.

Experimental

Assembly of LDH/C composites

The assembly of LDH/C composites was schematically shown in Scheme 1. In a typical run, $Ni(NO_3)_2{\cdot}6H_2O$ and $Al(NO_3)_3{\cdot}9H_2O$ were dissolved in deionized water to form a clear salt solution ($[Ni^{2+}] = 0.3$ M and $[Al^{3+}] = 0.1$ M). NaOH and Na_2CO_3 were dissolved in deionized water to form an alkali solution ($[OH^-] = 1.6[Ni^{2+} + Al^{3+}]$ and $[CO_3^{2-}] = 2[Al^{3+}]$). The above solutions were rapidly mixed in a colloid mill within several minutes. The resulting suspension was centrifuged, washed, and redispersed in deionized water for five cycles to obtain LDH precipitate. Glucose (analytical grade) was dissolved in deionized water to form a solution with a given molar ratio to total cations. The LDH precipitate was dispersed in the glucose solution, and then was transferred into an autoclave and maintained at 423 K for 10 h. The product was centrifuged and washed with deionized water and ethanol for five times, respectively. Finally, the precipitate was oven-dried at 343 K for 8 h to obtain NiAl-LDH/C composite. The samples were denoted as NA-C1, NA-C2.5, and NA-C5, in which the number denoted the molar ratio of glucose to starting total cations.

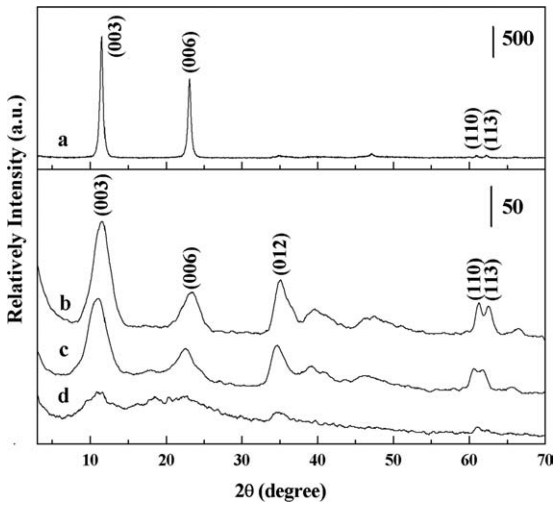

Figure 1. XRD patterns of (a) NA, (b) NA-C1, (c) NA-C2.5, and (d) NA-C5 composites.

The pure NiAl-LDH sample was synthesized in a similar process only with no addition of glucose upon hydrothermal crystallization (denoted as NA).

Formation of Ni nanoparticles

The composite samples were loaded into alumina boat and calcined in a tube furnace in a flowing N_2 atmosphere. The furnace was heated to a preset temperature at a rate of 5 K/min and maintained for 1 h. After reaction, the furnace was naturally cooled down to room temperature. Black powder was collected from alumina boat.

Catalytic growth of CNTs

The growth of CNTs was carried out in a tube furnace by chemical vapor deposition of acetylene (C_2H_2). Usually, tube-furnace reactor is suitable for a foundational experimental research, not for large-scale manufacturing, due to mass transfer limitation between carbonaceous gas and solid catalyst, limited amount of catalyst used and noncontinuous operation of tube furnace. In a typical synthesis of CNTs, LDH/C composite powder (0.30 g) was loaded into an alumina boat and placed in the middle of quartz tube inside the tube furnace. The furnace was ramped to 973 K at a rate of 5 K/min under N_2 flow (60 ml/min). The mixture gas of N_2/C_2H_2 (flow rate 10:1) was passed through after the furnace was held at 973 K for 1 h. The furnace was powered off after 1 h and naturally cooled down to room temperature. Finally, black product was collected from alumina boat. The samples were denoted as NA-C1-CNT, NA-C2.5-CNT, and NA-C5-CNT. The yield of carbon materials obtained was calculated as follows: yield (%) = (mass of carbon deposited onto the catalyst/mass of the reduced composite at 973 K) $\times$ 100. Also, the representative NA-C2.5-CNT was treated in a nitric acid solution of 6 M at 353 K for 8 h. The product was thoroughly washed by deionized water till neutral pH and then dried in an oven at 333 K overnight.

Characterization

Powder X-ray diffraction (XRD) patterns of the samples were collected using a Shimadzu XRD-6000 diffractometer (conditions: 40 kV, 30 mA, graphite-filtered CuKα radiation, and $\lambda = 0.15418$ nm).

Room-temperature Fourier transform infrared (FTIR) spectra were recorded on a Bruker Vector-22 Fourier transform spectrometer over the wavelength range 4000–400 cm^{-1} with a resolution of 2 cm^{-1}. The samples were prepared by KBr pellet method.

Elemental analyses (C and H content) were carried out using an elemental analyzer (Elementarvario EL) with an instrumental sensitivity of 0.3%.

Thermogravimetric and differential thermal analysis (TG-DTA) were carried out using a Perkin-Elmer Diamond thermal analysis system under flowing nitrogen at the ramping rate of 10 K/min.

The microstructure of product was observed by Hitachi H-800 transmission electron microscopy (TEM, accelerating voltage of 200 kV) and high-resolution transmission electron microscopy (HRTEM, JEOL2010, 200 kV). Before TEM observations, small amount of sample was ultrasonically dispersed in ethanol to obtain a suspension, and a drop of the resulting suspension was deposited on a carbon-coated fine-mesh Cu grid followed by the evaporation of solvent in air.

The specific surface area measurements were carried out using a BET method from N_2-sorption at 77 K on a static volumetric Quantachrome Autosorb-1C-VP Analyzer. For accuracy, the measurement for each sample was repeated thrice. Before the measurements, samples were degassed at 473 K for a period of 4 h.

X-ray photoelectron spectra (XPS) was recorded on a Thermo VG ESCALAB250 X-ray photoelectron spectrometer at a base pressure of 2×10^{-9} Pa using Al Kα X-ray as the excitation source (1486.6 eV).

The Raman spectra were collected at room temperature using a Jobin Yvon Horiba HR800 Raman spectrometer. The excitation source comes from a laser of 532 nm wavelength.

Results and Discussion

Characterization of hybrid LDH/C composites

XRD patterns of LDH and hybrid LDH/C composites were shown in Figure 1. The pattern of NA sample (Figure 1a) presents the characteristic (003), (006), (110), and (113) reflections, corresponding to layered hydrotalcite-like compounds.[2] The intensive reflections reveal highly crystalline nature of product. In comparison, the patterns of composites show a broadening feature of reflections, although the reflections appear in the same positions as those of NA. It is noted that the reflection intensity of LDH greatly weakens (indicated by the scale) and the structural integrity of LDH phase decreases with increasing molar ratio of starting glucose to cations (Figures 1b–d). Further, the structural integrity of LDH phase in the composite, which is defined as the crystalline nature of LDH phase, may be quantified by the ratio of reflection (003) full width at half maximum (FWHM) of pure LDH sample to that of LDH phase in composites (Table 2). The smaller is the ratio, the lower is the structural integrity of LDH phase. However, it is difficult to accurately

Table 1. Comparison on Structural Parameters of NA and NA-C2.5

Parameters	Sample	
	NA	NA-C2.5
d(003)/nm	0.7683	0.8096
d(006)/nm	0.3851	0.3948
d(110)/nm	0.1518	0.1530
Lattice parameter,* a/nm	0.3036	0.3060
Lattice parameter, c/nm	2.3049	2.4288
Crystallite size† in a direction (D_{110})/nm	30	13
Crystallite size in c direction (D_{003})/nm	17	3.5

*$a = 2d(110)$, $c = 3d(003)$.
†Crystallite sizes calculated by Scherer's formula.

calculate the structural integrity of LDH in NA-C5 sample due to the severe broadening of the reflection. The aforementioned results can be attributed to the diluent effect of resultant carbon in the composite materials. Furthermore, it is found that no reflections related to graphite or other forms of carbon appeared in the pattern, indicative of the presence of carbon in noncrystalline form in the composite. It is well-documented that the aromatization and carbonization of glucose can take place under the present hydrothermal conditions.[42] As a result, the resultant carbon was assembled with LDH crystallites forming simultaneously through the crystallization of LDH nuclei, leading finally to the formation of hybrid LDH/C composites. The detailed structural parameters of NA and NA-C2.5 were listed in Table 1. It can be seen that the $d_{(003)}$ value for NA-C2.5 (0.8096 nm) is larger than that for NA (0.7683 nm) with interlayer carbonate anions. The expansion of $d_{(003)}$ spacing suggests that some organic species from the initial aromatization of glucose are likely intercalated into the interlayer of LDH. According to Scherrer's formula, the crystallite sizes in c and a directions (D_{003} and D_{110}) decreased from 17–30 nm for sample NA to 3.5–13 nm for NA-C2.5 sample, respectively. The remarkable decrease in crystallite size of LDH can be attributed to the confined effect of carbon on the growth of LDH crystallites during the hydrothermal assembly.

Figure 2 shows FTIR spectra of LDH and LDH/C composites in the region between 4000 cm^{-1} and 500 cm^{-1}. For NA sample (Figure 2a), a broad absorption band at 3600–3350 cm^{-1} can be assigned to the O—H stretching vibration (υ_{O-H}) of hydroxyl groups within brucite-like layers and intercalated water molecules. The absorption at 1643 cm^{-1} originates from the O—H bending vibration (δ_{O-H}) of hydroxyl groups. The other absorption bands peaked at 1369 cm^{-1} and 743 cm^{-1} correspond to the symmetric stretching vibration (υ_{C-O}) and bending vibration (δ_{C-O}) of CO_3^{2-}, respectively, arising from the intercalated carbonate ion within LDH.[43] For LDH/C composites (Figures 2b–d), the absorptions associated to both LDH and carbon can be detected. In addition to the absorptions associated to LDH (υ_{O-H} and υ_{C-O}), the newly appeared band at 1612 cm^{-1} results from the C=C asymmetric stretching vibration ($\upsilon_{C=C}$) of carbon.[44] The weak absorption within the range of 1000–1100 cm^{-1} is attributable to C—OH stretching and O—H bending vibrations, indicative of the presence of hydroxyl groups associated with carbon. Although the vibrations assigned to —OH and CO_3^{2-} of LDH itself are retained, the intensities of vibrations remarkably weaken in the composites because of the hybrid characteristic of the composite. It can be seen that the intensity ratio of $\upsilon_{C=C}$ to υ_{C-O} increases from NA-C1 to NA-C5 (Figures 2b–d), proving an increasing amount of carbon in the composite. Furthermore, elemental analyses determine the content of carbon and hydrogen in pure LDH and LDH/C composites, indicative of the carbon-rich characteristic of the composite and the increasing carbon content from NA-C1 to NA-C5 (Table 2).

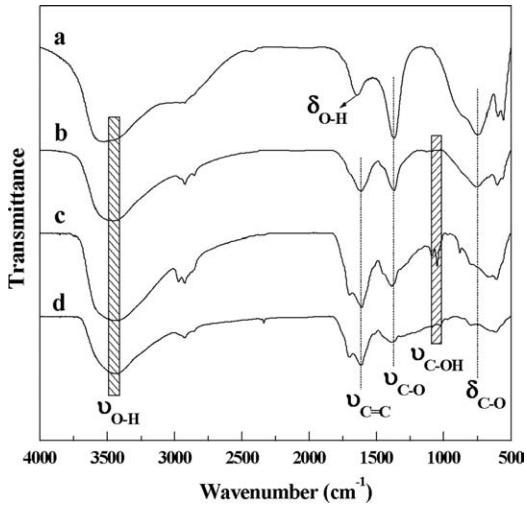

Figure 2. FTIR spectra of (a) NA, (b) NA-C1, (c) NA-C2.5, and (d) NA-C5 composites.

The morphology of LDH and LDH/C composites was examined and compared by microscope observation. SEM image of NA shows platelet-like particles with lateral dimension ranging from 80 to 120 nm (Figure 3a). Most of the particles present hexagonal external shape, which is a common feature of well-crystallized LDH materials. In comparison, the composites display distinctly different morphology from LDH (Figures 3b–d). A hybrid structure is presented in these samples instead of well-crystallized platelet-like LDH particles. It is difficult to distinguish the exact shape and size of LDH particles because of the interwoven characteristic of LDH and amorphous carbon. Further, TEM photograph clearly shows that NA possesses platelet feature and large width-to-thickness ratio, confirming the two-dimensional crystallography of LDH itself (Figure 4a). However, the composite in the case of NA-C2.5 presents a highly hybridized feature, as shown in Figure 4b. No platelet-like crystallites were observed in the composite. The NA-C1 and NA-C5 samples display an identical morphology to that of NA-C2.5 (not shown). The aforementioned results clearly indicate that the hydrothermal assembly involving the

Table 2. Elemental Analyses and Structural Integrity of LDH/C Composites and LDH

Sample	C (wt %)	H (wt %)	Ratio*
NA	2.606	3.275	1.0
NA-C1	20.82	4.783	0.2037
NA-C2.5	37.27	4.735	0.2028
NA-C5	49.96	5.856	–

*The ratio of reflection (003) FWHM of pure LDH sample to that of LDH in composites.

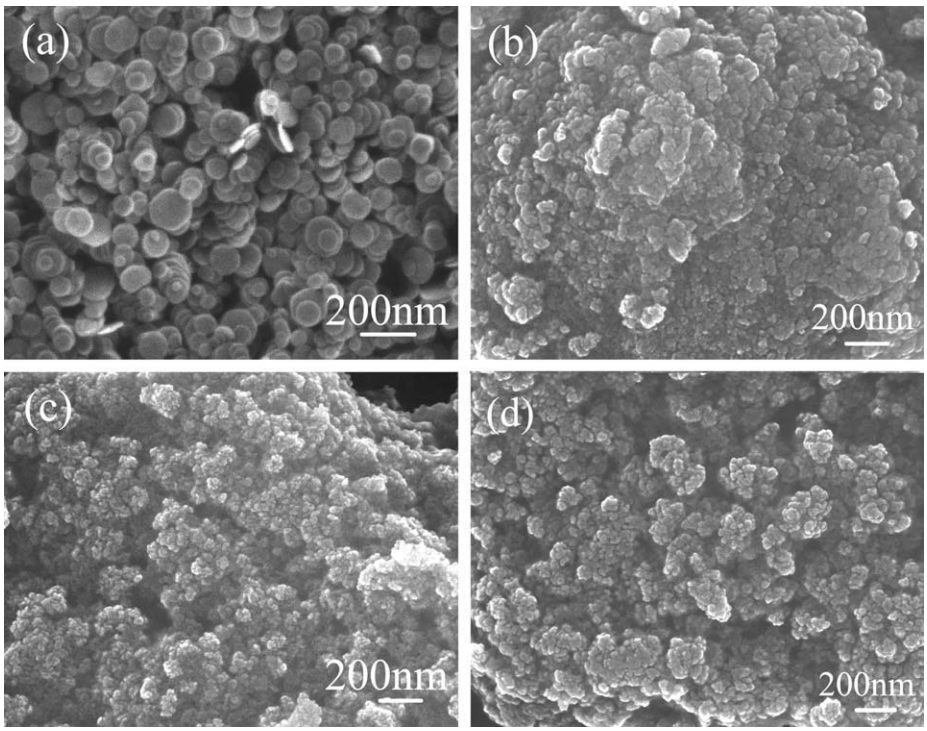

Figure 3. SEM images of (a) NA, (b) NA-C1, (c) NA-C2.5, and (d) NA-C5 composites.

crystallization of LDH and carbonization of glucose leads to an interwoven hybrid structure consisting of LDH particles and noncrystalline carbon. It is expected that such a hybrid could prevent the particles from agglomerating upon thermal conversion of LDH phase.

The thermal behavior of LDH (NA) and composite (NA-C2.5) is studied under an inert atmosphere by TG-DTA. It is known that the weight loss events essentially occur in two stages for LDH, which are accompanied with two endothermic peaks.[2] The first one is assigned to the removal of adsorbed water on the outer surface of crystallites and hydrate molecules in the interlayer, corresponding to an endothermic peak at 498 K (Figure 5a). The second one involves both dehydroxylation of the layers and the loss of intercalated CO_3^{2-}, showing an endothermic effect peaked at 622 K. The slight weight loss after 673 K is ascribed to the removal of strongly bonded hydroxyl groups onto brucite-like LDH layers. In contrast, the NA-C2.5 sample shows a distinguished thermal behavior (Figure 5b). The first endothermic effect with a maximum at 465 K is ascribed to the elimination of physisorbed and intercalated water molecules in LDH. The negative shift of endothermic peak (ca. 33 K) could owe to the decreasing ratio of LDH in the composite. The second one peaked at 654 K originates from dehydroxylation and decarbonate of LDH and as well the removal of hydroxyl groups associated with carbon, which is 32 K higher than that of NA. The shift to higher temperature is possibly due to the interaction between hybridized carbon and LDH, leading to stronger bondage of thermally volatile species within LDH. The weight loss event from 723 to 973 K involves multiendothermic peaks, which can be attributable to the stepwise reduction of Ni^{2+} cations by carbon.

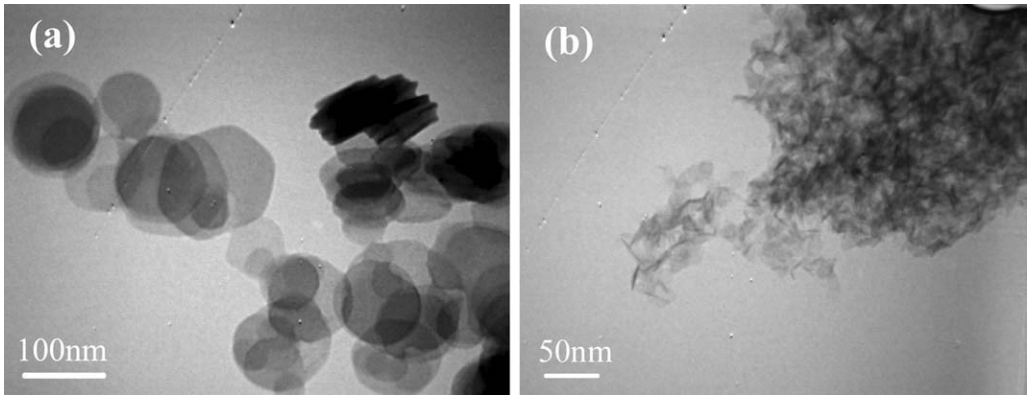

Figure 4. TEM photographs of (a) NA and (b) NA-C2.5 composite.

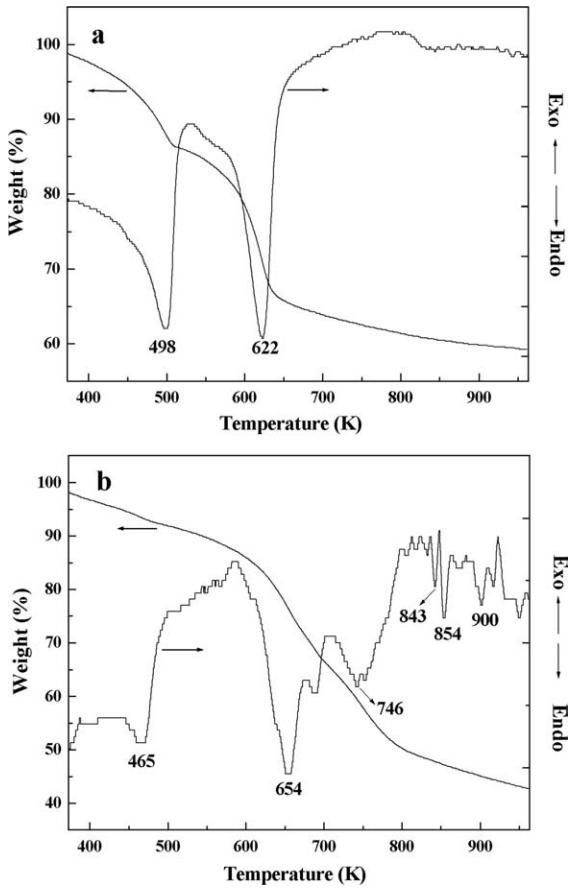

Figure 5. TG-DTA curves of (a) NA and (b) NA-C2.5 composite under N_2 atmosphere.

The multipeaks indicate that the reduction reactions occur covering a broad range of temperature.

Structure of supported Ni nanoparticles

To obtain supported Ni nanoparticles, the LDH/C composite was treated under different temperature in flowing N_2 atmosphere. In the case of NA-C2.5, XRD pattern of calcined products at 773 K shows the dominant NiO phase and no detectable Ni phase (Figure 6a). On elevating temperature to 873 K, the main contribution of reflections arises from metallic Ni (Figure 6b), which can be indexed to fcc Ni phase (JCPDS No. 87-0712). NiO phase can also be detected in this pattern although the intensities are greatly decreased compared with those in Figure 6a. This indicates that phase transformation from NiO to Ni apparently occurs at the temperature owing to the reduction of NiO. The pattern in Figure 6c shows only fcc Ni phase upon further increasing temperature to 973 K, and the reflections corresponding to NiO phase do not appear. It is well-known that upon calcination at appropriate intermediate temperatures (723–873 K) under air or under an inert atmosphere, LDH loses the pristine-layered structure and transforms into the corresponding poorly crystallized mixed metal oxides with large specific surface areas and homogeneous dispersion of the metal components at an atomic level, which are suitably used as catalysts or catalyst supports.[2,9] However, calcination above 1023 K is known to give a large amount of spinel-type complex metal oxides with decreased specific surface areas.[45] Therefore, calcination temperature has a marked effect on the textural feature and composition of the resulting materials. Nevertheless, NA-C2.5 composite treated in N_2 atmosphere results in metallic Ni phase. This suggests that the resulting metal oxides from thermal decomposition of LDH can be reduced into metal under appropriate conditions. Because no reducing atmosphere is additionally introduced into the reaction system, carbon in the composite plays a role of reducing agent, leading to in situ reduction of Ni^{2+} cations. The main reduction reactions occurred can be expressed as follows:

$$NiO + C(s) \rightarrow Ni + CO(g) \quad (1)$$

$$NiO + CO(g) \rightarrow Ni + CO_2(g) \quad (2)$$

The calcined product at 973 K contained no detectable NiO phase, indicative of the complete reduction from NiO to metallic Ni. Additionally, the patterns of products by calcination of NA-C1 and NA-C5 under identical conditions show that only Ni is XRD-detectable phase (Figures 6d, e) similar to that of Figure 6c. This suggests that the reduction reaction can take place in a wide range of carbon content. On heating, LDH is transformed into mixed oxides (crystalline NiO and amorphous alumina). Simultaneously, the carbon around NiO phase can act as a reducing agent, leading to in situ self-reduction of NiO to metallic Ni. Correspondingly, the reduced Ni particles are exposed due to the depletion of the surrounding carbon. After reduction, the residual carbon as one of support or dispersing matrices can prevent Ni particles from agglomeration. The higher carbon content in composites results in more residual carbon, thus giving rise to a better dispersion of the reduced Ni particles. In this case, the carbon deposition on Ni particles does not remarkably take place. The estimated crystallite size (D_{111}) of Ni

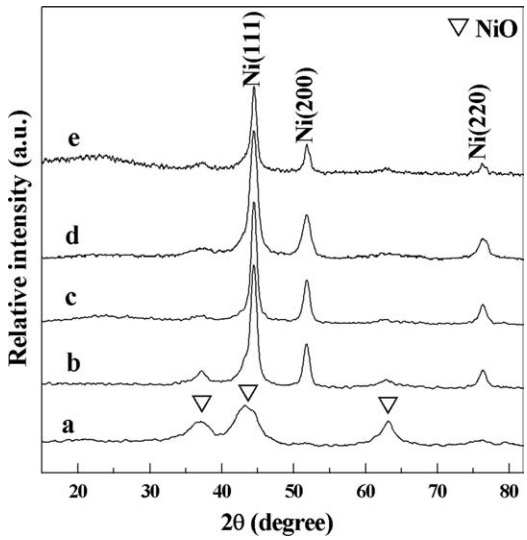

Figure 6. XRD patterns of products obtained from NA-C2.5 calcined at (a) 773 K, (b) 873 K, (c) 973 K, and products from (d) NA-C1 and (e) NA-C5 calcined at 973 K.

Table 3. Crystallite Sizes (D_{hkl})* of Ni for the Composite Reduced at 973 K

Sample	Miller Index (*hkl*)	D_{hkl}/nm
NA-C1	111	7.0
	200	7.5
NA-C2.5	111	9.5
	200	9.7
NA-C5	111	10.1
	200	10.4

*Crystallite sizes calculated by Scherer's formula.

based on Scherrer's formula is 7.0, 9.5, and 10.1 nm for products from NA-C1, NA-C2.5, and NA-C5, respectively, and the crystallite size (D_{200}) of Ni presents the same tendency with carbon content (Table 3). The estimated crystallite size of Ni particles slightly increases with the carbon content. This is because that the resultant NiO can be reduced more easily upon the presence of more surrounding carbon, thus slightly larger Ni particles can be formed. However, the calculated sizes of Ni particles for NA-C2.5 (9.5 nm) and NA-C5 (10.1 nm) have a minor difference. This suggests that the Ni particle size is less affected by carbon content in the presence of excessive carbon.

The dispersion state of reduced Ni particles was characterized by TEM observations. Figures 7a–c exhibit TEM photographs of Ni nanoparticles produced from NA-C1, NA-C2.5, and NA-C5 calcined at 973 K. On less carbon content, slight aggregates occasionally appear and the reduced Ni particles remain small sizes of about 8–10 nm. The Ni nanoparticles (dark contrast) show excellent dispersion in amorphous alumina and carbon matrix with increasing carbon (Figure 7b). The matrix is more clearly presented in Figure 7c, in which Ni nanoparticles still remain high dispersion. The BET specific surface area of reduced products is 98 ± 4 for NA-C1, 151 ± 4 for NA-C2.5, and 202 ± 6 m^2 g^{-1} for NA-C5, which shows an increasing tendency with carbon content. The higher carbon content in the composites leads to higher BET specific surface area owing to larger pore volume evolved during the depletion of carbon. HRTEM image, in the case of Ni nanoparticles from NA-C2.5, clearly shows lattice fringes corresponding to plane (111) of fcc Ni with a *d*-spacing of 0.204 nm (Figure 7d). It is interestingly noted that the image presents two adjacent particles, indicating that the neighboring growth may take place during the formation of Ni crystallites due to large amount of Ni. Additionally, well-graphitized layers (or shells) and lattice fringes are not observed in the surroundings of Ni nanoparticles, suggestive of the nature of amorphous alumina and/or disordered carbon residue. This is well-consistent with the XRD results (Figure 6c). The aforementioned structural characterization of materials reveals that highly dispersed Ni nanoparticles with homogeneous size can be produced via the self-reduction of LDH/C nanocomposites on the basis of a highly hybridized structure of small LDH crystallites and carbon. It is generally believed that high dispersion of metal nanoparticles is critical in achieving excellent performance. Correspondingly, as-synthesized supported Ni catalysts should exhibit good catalytic property for the growth of CNTs.

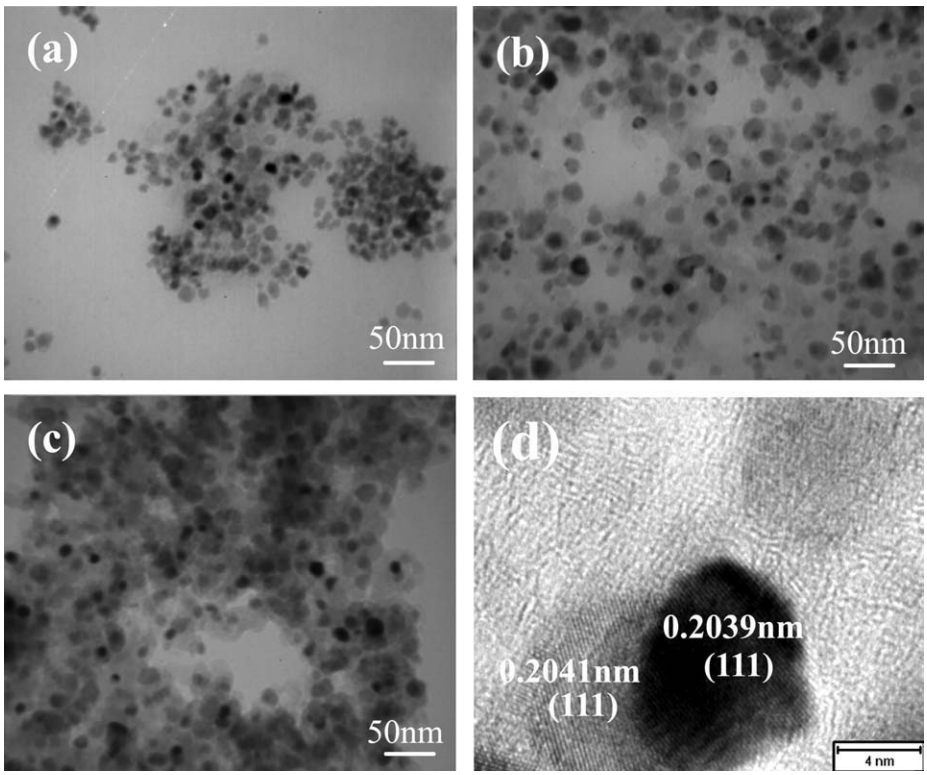

Figure 7. TEM photographs of supported Ni catalysts produced at 973 K from (a) NA-C1, (b) NA-C2.5, and (c) NA-C5, and (d) HRTEM image of Ni nanoparticles from NA-C2.5.

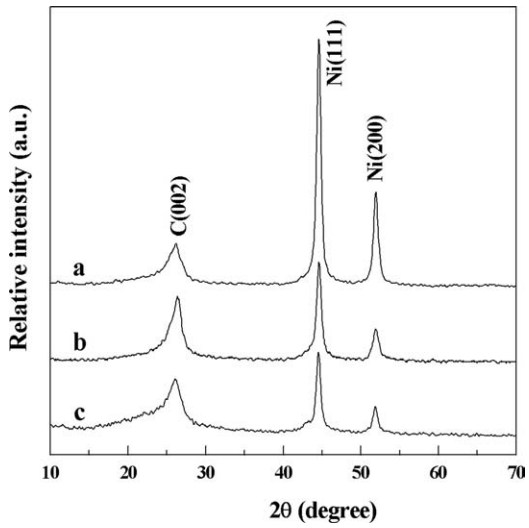

Figure 8. XRD patterns of (a) NA-C1-CNT, (b) NA-C2.5-CNT, and (c) NA-C5-CNT.

Catalytic growth of CNTs

The growth of CNTs was carried out by CVD of acetylene for evaluating the catalytic performance of supported Ni nanoparticles. Herein, CNTs were directly grown over LDH/C composite via an integrated process, which involves no separate calcination and reduction steps. Figure 8 shows XRD patterns of CNTs over NA-C1, NA-C2.5, and NA-C5. The reflection at about 26.2° can be assigned to that of graphite (002), suggestive of the formation of graphite phase in all the three samples. The *d*-spacing values of graphite (002) are 0.339–0.342 nm for three samples, larger than that for the graphite one (0.3354 nm). This indicates that the structural distortion took place during the curling and stacking of graphene layers.[46] The other two reflections at 4.6° and 51.9° can be indexed to fcc Ni (111) and (200), respectively (JCPDS No. 87-0712). In addition, no reflections related to metal oxides or spinels were detected, indicating that no other crystalline phases exist in the product. According to Scherrer's formula, the crystallite size $D_{Ni(111)}$ is estimated to be 14.5 nm, 12.5 nm, and 14.6 nm for NA-C1-CNT, NA-C2.5-CNT, and NA-C5-CNT, respectively. There is a minor difference among the crystallite sizes. This indicates that agglomeration of Ni crystallites hardly takes place during the deposition of carbonaceous gas, proving the high dispersion and stabilization of Ni particles. It is noted that the relative intensity of $I_{Ni(111)}/I_{C(002)}$ for NA-C1-CNT is higher than those for NA-C2.5-CNT and NA-C5-CNT. This suggests that the NA-C1-CNT contains less-graphitized component due to the relationship between relative intensity and phase compositions.

The morphology and microstructure of the products were characterized by TEM. The hollow tubular nanostructures can be observed confirming the formation of nanotubes. The nanotubes have diameters in the range of about 10–18 nm for the three samples (Figure 9). Three is a minor difference in diameters of CNTs among the three samples because of similar sizes of reduced Ni nanoparticles. It is worth noting that few large-sized particles are observed, suggestive of the absence of oxide or spinel residues, as confirmed by XRD. For NA-C1-CNT, HRTEM observation reveals that the CNTs have the characteristic of multiwalled nanotubes (Figure 9d). The intershell distance of nanotubes (~0.340 nm) is slightly larger than that of graphitic (002). The defects and imperfectly graphitized layers exist within the side-walls and the interior of nanotubes (pointed by arrows), suggestive of the disordered stacking or distortion of graphene layers occurred during the decomposition and deposition of carbonaceous gas. The amorphous coatings can also be found outside the nanotube, typically highlighted by straight lines. NA-C2.5-CNT presents relatively straight tubular morphology (Figure 9b), whereas NA-C5-CNT shows a lot of kinked nanotubes, thus resulting in intertwisted morphology (Figure 9c). The nanotubes in NA-C2.5-CNT have a wall thickness of about 2.7 nm and interlayer spacing (0.339 nm) (Figure 9e). The NA-C5-CNT shows a similar wall thickness and interlayer spacing (Figure 9f). Furthermore, most of the nanotubes present a hollow channel and head without entrapped metal particles. This reveals that a base-growth mode of nanotubes is dominant owing to strong interaction between active metal particles and support.[21] This suggests that after purification, the Ni nanoparticles on support can be removed more easily than those encapsulated within the nanotubes via a tip-growth mode. TEM observations of purified NA-C2.5-CNT product (see Supporting Information Figure S1) verify that most of metal impurities have been eliminated, and almost every nanotube shows hollow channel and head. It confirms that high-purity CNTs have been obtained after purification.

In addition, the calculated yield of carbon materials over NA-C1, NA-C2.5, and NA-C5 is about 321, 776, and 1029%, respectively, presenting an increasing tendency in carbon yield. This is due to the improved dispersion of reduced Ni nanoparticles with carbon content in LDH/C composites, leading to the enhanced catalytic activity. Furthermore, the increasing BET surface area of catalysts with the carbon content can facilitate the production of CNTs. According to thermogravimetric curves (see Supporting Information Figure S2), the weight loss of products in the range of 473–673 K comes from the removal of amorphous carbon because of its lower activation energy for oxidation.[47] Correspondingly, the weight percentage of amorphous carbon in products is no more than 1.3%. Consequently, the nanotube structure is definitely dominant in all products. Additionally, to investigate the reproducibility of catalyst preparation and CNT synthesis, the supported Ni catalysts were repeatedly synthesized under identical conditions for several times and further used for the growth of CNTs. It is found that the diameters and distributions of CNTs obtained using fresh catalysts keep almost the same by TEM observation, and the yields of carbon materials have a deviation within about 5% indicating that both catalyst manufacture and CNT syntheses are well-reproducible.

On the other side, we carried out the growth of CNTs over pure NiAl-LDH sample. It is found from TEM photographs (see Supporting Information Figure S3) that only a few amounts of nanotubes can be observed, and the obtained carbon material is mainly composed of stacked carbon segments. Moreover, some catalyst particles were encapsulated by carbon deposition from thermolysis of C_2H_2. This could

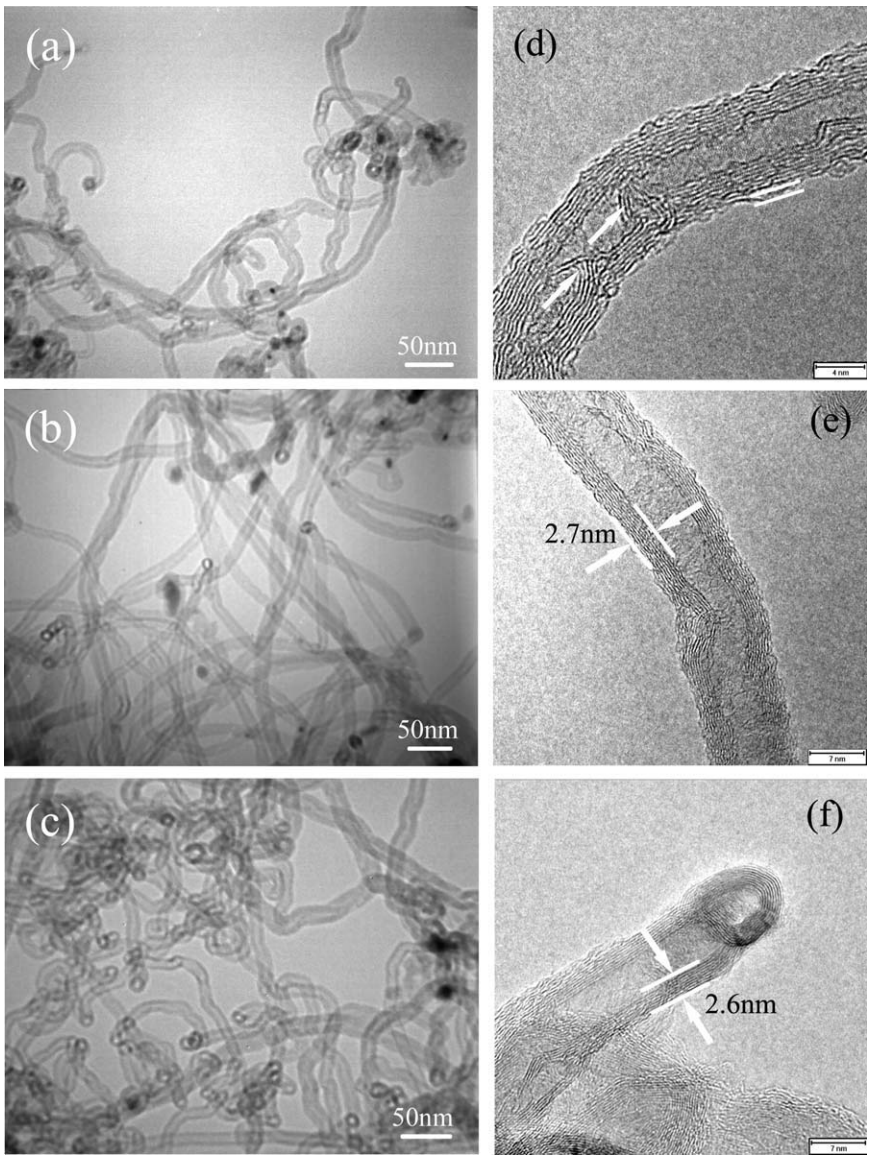

Figure 9. TEM photographs of (a) NA-C1-CNT, (b) NA-C2.5-CNT, (c) NA-C5-CNT and HRTEM images of (d) NA-C1-CNT, showing characteristic of multiwalled nanotube, (e) NA-C2.5-CNT, presenting the wall thickness of about 2.7 nm, and (f) NA-C5-CNT, displaying hollow body and head and the same wall thickness as that of NA-C2.5-CNT.

be due to the formation of large and nonuniform Ni particles (15–30 nm) during CVD process. The results further reveal that there is a great improvement on the growth of high-quality CNTs over LDH/C composites compared with pure NiAl-LDH sample.

The surface characteristic of synthesized carbon materials was studied by XPS technique. The shift of all binding energies was corrected using the C1s core level at 284.6 eV as an internal standard. All spectra have been fitted into a dominant peak of sp^2 carbon of graphite (284.6 $\pm$ 0.2 eV) and three peaks centered at 285.6 $\pm$ 0.2, 287.5 $\pm$ 0.2, and 289.7 $\pm$ 0.2 eV (Figure 10). The peak at 284.6 eV is assigned to the graphitic carbon and the one at 285.6 eV is attributed to sp^3 carbon or defects of nanotubes.[48,49] The peaks at higher-binding energies of 287.5 and 289.7 eV can be assigned as >C=O and —COO species, respectively.[50] The peak intensity was calculated based on the area of each peak in percentage of total C1s area. The peak intensity assigned to graphite and defect can be used to estimate the graphitization or disorder of CNTs in the three samples. It is noted that the intensity of graphite is lowest and the one of defect is highest for NA-C1-CNT (Table 4). This suggests that the sample has lower degree of graphitization or more defects than the other two samples. The NA-C2.5-CNT and NA-C5-CNT have close intensity values for the two peaks, which indicate that they possess nearly equivalent graphitization or quantity of defects on the surface of CNTs.

Raman spectroscopy was used to characterize the microstructural nature of carbon materials. Two vibration bands at about 1340–1345 and 1590–1596 cm^{-1} are ascribed to the D

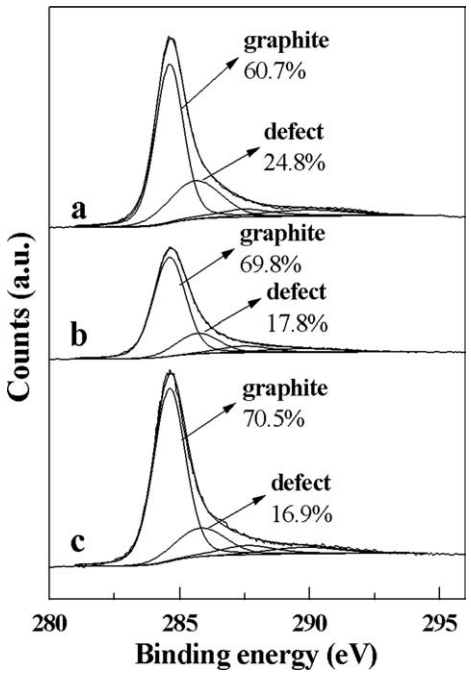

Figure 10. Deconvoluted C1s core level spectra of (a) NA-C1-CNT, (b) NA-C2.5-CNT, and (c) NA-C5-CNT.

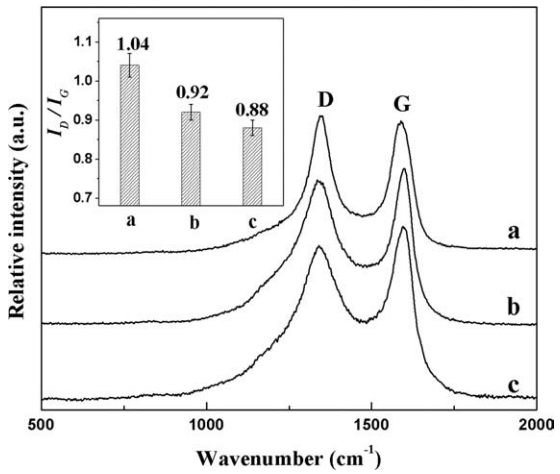

Figure 11. Raman spectra of (a) NA-C1-CNT, (b) NA-C2.5-CNT, and (c) NA-C5-CNT (Inset shows the values of I_D/I_G for three samples).

and G band of the graphitized CNTs, respectively, for all three samples (Figure 11). The D band originates from the structural disorder within the nanotubes or the amorphous carbon. The G band is associated with the vibration of sp^2-hybridized carbon atoms in a two-dimensional hexagon lattice, indicative of the formation of ordered graphene layers.[51] Usually, the ratio (I_D/I_G) is used for evaluating the stack ordering of graphene layers within CNTs.[52] The larger I_D/I_G is, the lower degree of graphitization is. It can be estimated from the spectra that the I_D/I_G value is 1.04, 0.92, and 0.88 for NA-C1-CNT, NA-C2.5-CNT, and NA-C5-CNT, respectively. The errors of I_D/I_G value for these samples are shown in the inset of Figure 11 based on 10 Raman spectrum spots. It is noted that the NA-C1-CNT shows the lowest degree of graphitization, that is, more defects or structural disorder than the other two samples. The close I_D/I_G values for NA-C2.5-CNT and NA-C5-CNT are attributed to the similar structure of nanotubes, such as diameters and wall thickness. The overall microstructure of CNTs is slightly improved in the NA-C5-CNT according to I_D/I_G value, indicative of a positive effect of more carbon residue on the structural ordering of as-grown CNTs. The results are consistent with those evidenced by XPS.

As a result, the yield of CNTs presents an increasing tendency with carbon content in LDH/C composites, and the quality of CNTs is slightly improved from NA-C2.5-CNT to NA-C5-CNT. Therefore, it is expected that high-quality CNTs having higher yields can be synthesized using optimal carbon contents in LDH/C composites. The further detailed investigation needs to be carried out.

Conclusions

The NiAl-LDH/C composites with adjustable carbon content were assembled via crystallization of LDH in combination with hydrothermal carbonization of glucose. The controlled conversion of the composites under an inert atmosphere resulted in highly dispersive supported Ni nanoparticles with the average size of about 10 nm, owing to the hybrid characteristic of LDH/C composites and reducing ability of carbon component in the composites. The degree of reduction for metallic Ni significantly depended on reduction temperature. The sizes of reduced Ni nanoparticles increased slightly with the carbon content in the composite. Furthermore, LDH/C composites exhibited excellent catalytic performance for growth of multiwalled CNTs via an integrated process. The structural ordering of as-prepared CNTs can be delicately tuned by adjusting the carbon content in the LDH/C composites. More importantly, due to the tunability of cations within LDH layers, it is expected that the synthesis strategy reported here can be flexibly extended to fabricate a variety of supported metal nanoparticle catalysts with interesting catalytic properties based on a facile and

Table 4. Binding Energy and Peak Intensity of Deconvoluted C1s Core Level for CNTs

	Binding Energy (eV)				Peak Intensity (%)	
Sample	Graphite	Defect	>C=O	—COO	Graphite*	Defect†
NA-C1-CNT	284.6	285.6	287.5	289.9	60.7	24.8
NA-C2.5-CNT	284.6	285.7	287.5	289.7	69.8	17.8
NA-C5-CNT	284.6	285.8	287.6	289.8	70.5	16.9

*Intensity of graphite in percentage of total C1s area.
†Intensity of defect in percentage of total C1s area.

controllable assembly of LDH/C composite, for example, CoAl-LDH/C, NiCuAl-LDH/C, and CuZnAl-LDH/C. This synthesis route described shows the merits of ease, flexibility, and versatility for supported metal nanoparticles and opens up new possibilities of promising catalysis application for such materials.

Acknowledgments

The authors acknowledge the financial support from the National Natural Science Foundation of China, 973 Program (2009CB939802), the Program for Changjiang Scholars and Innovative Research Team in University (CSIRT0406), and the 111 Project (B07004).

Literature Cited

1. Braterman PS, Xu ZP, Yarberry F. In: Auerbach SM, Carrado KA, Dutta PK, editors. *Handbook of Layered Materials*. New York: Marcel Dekker, 2004:373–474; Chapter 8: Layered Double Hydroxides (LDHs).
2. Evans DG, Slade RCT. Structural aspects of layered double hydroxides. *Struct Bonding*. 2006;119:1–87.
3. Williams GR, O'Hare D. Towards understanding, control and application of layered double hydroxide chemistry. *J Mater Chem*. 2006;16:3065–3074.
4. Zhang F, Xiang X, Li F, Duan X. Layered double hydroxides as catalytic materials: recent development. *Catal Surv Asia*. 2008;12:253–265.
5. Tang Y, Liu Y, Zhu P, Xue Q, Chen L, Lu Y. High-performance HTLcs-derived CuZnAl catalysts for hydrogen production via methanol steam reforming. *AIChE J*. 2009;55:1217–1228.
6. Lei XD, Zhang FZ, Yang L, Guo XX, Tian YY, Fu SS, Li F, Evans DG, Duan X. Highly crystalline activated layered double hydroxides as solid acid-base catalysts. *AIChE J*. 2007;53:932–940.
7. Wei M, Zhang X, Evans DG, Duan X. Rh-TPPTS intercalated layered double hydroxides as hydroformylation catalyst. *AIChE J*. 2007;53:2916–2924.
8. Yang L, Shahrivari Z, Liu PKT, Sahimi M, Tsotsis TT. Removal of trace levels of arsenic and selenium from aqueous solutions by calcined and uncalcined layered double hydroxides (LDH). *Ind Eng Chem Res*. 2005;44:6804–6815.
9. Evans DG, Duan X. Preparation of layered double hydroxides and their applications as additives in polymers, as precursors to magnetic materials and in biology and medicine. *Chem Commun*. 2006;485–496.
10. Tsyganok AI, Tsunoda T, Hamakawa S, Suzuki K, Takehira K, Hayakawa T. Dry reforming of methane over catalysts derived from nickel-containing Mg-Al layered double hydroxides. *J Catal*. 2003;213:191–203.
11. Gérardin C, Kostadinova D, Sanson N, Coq B, Tichit D. Supported metal particles from LDH nanocomposite precursors: control of the metal particle size at increasing metal content. *Chem Mater*. 2005;17:6473–6478.
12. Gérardin C, Kostadinova D, Coq B, Tichit D. LDH nanocomposites with different guest entities as precursors of supported Ni catalysts. *Chem Mater*. 2008;20:2086–2094.
13. Olafsen A, Daniel C, Schuurman Y, Råberg LB, Olsbye U, Mirodatos C. Light alkanes CO_2 reforming to synthesis gas over Ni based catalysts. *Catal Today*. 2006;115:179–185.
14. Resini C, Montanari T, Barattini L, Ramis G, Busca G, Presto S, Riani P, Marazza R, Sisani M, Marmottini F, Costantino U. Hydrogen production by ethanol steam reforming over Ni catalysts derived from hydrotalcite-like precursors: catalyst characterization, catalytic activity and reaction path. *Appl Catal A*. 2009;355:83–93.
15. Olafsen A, Slagtern Å, Dahl IM, Olsbye U, Schuurman Y, Mirodatos C. Mechanistic features for propane reforming by carbon dioxide over a Ni/Mg(Al)O hydrotalcite-derived catalyst. *J Catal*. 2005;229:163–175.
16. Qi C, Amphlett JC, Peppley BA. Product composition as a function of temperature over NiAl-layered double hydroxide derived catalysts in steam reforming of methanol. *Appl Catal A*. 2006;302:237–243.
17. Verónica M, Graciela B, Norma A, Miguel L. Ethanol steam reforming using Ni(II)-Al(III) layered double hydroxide as catalyst precursor—kinetic study. *Chem Eng J*. 2008;138:602–607.
18. Iijima S. Helical microtubules of graphitic carbon. *Nature*. 1991;354:56–58.
19. Thess A, Lee R, Nikolaev P, Dai H, Petit P, Robert J, Xu C, Lee YH, Kim SG, Colbert DT, Scuseria G, Tomanek D, Fisher JE, Smalley RE. Crystalline ropes of metallic carbon nanotubes. *Science*. 1996;273:483–487.
20. Kitiyanan B, Alvarez WE, Harwell JH, Resasco DE. Controlled production of single-wall carbon nanotubes by catalytic decomposition of CO on bimetallic Co-Mo catalysts. *Chem Phys Lett*. 2000;317:497–503.
21. Dupuis AC. The catalyst in the CCVD of carbon nanotubes-a review. *Prog Mater Sci*. 2005;50:929–961.
22. See CH, Harris AT. A review of carbon nanotube synthesis via fluidized-bed chemical vapor deposition. *Ind Eng Chem Res*. 2007;46:997–1012.
23. Philippe R, Serp P, Kalck P, Kihn Y, Bordère S, Plee D, Gaillard P, Bernard D, Caussat B. Kinetic study of carbon nanotubes synthesis by fluidized bed chemical vapor deposition. *AIChE J*. 2009;55:450–464.
24. Kathyayini H, Nagarajua N, Fonseca A, Nagy JB. Catalytic activity of Fe, Co and Fe/Co supported on Ca and Mg oxides, hydroxides and carbonates in the synthesis of carbon nanotubes. *J Mol Catal A: Chem*. 2004;223:129–136.
25. Jeong HJ, Kim KK, Jeong SY, Park MH, Yang CW, Lee YH. High-yield catalytic synthesis of thin multiwalled carbon nanotubes. *J Phys Chem B*. 2004;108:17695–17698.
26. Son SY, Lee Y, Won S, Lee DH, Kim SD, Sung SW. High-quality multiwalled carbon nanotubes from catalytic decomposition of carboneous materials in gas-solid fluidized beds. *Ind Eng Chem Res*. 2008;47:2166–2175.
27. Wang Y, Wei F, Luo G, Yu H, Gu G. The large-scale production of carbon nanotubes in a nano-agglomerate fluidized-bed reactor. *Chem Phys Lett*. 2002;364:568–572.
28. Yu H, Zhang Q, Wei F, Qian W, Luo G. Agglomerated CNTs synthesized in a fluidized bed reactor: agglomerate structure and formation mechanism. *Carbon*. 2003;41:2855–2863.
29. Keller TM, Laskoski M, Qadri SB. Ferrocene catalyzed carbon nanotube formation in carbonaceous solid. *J Phys Chem C*. 2007;111:2514–2519.
30. Pang WW, Lim S, Zhang YZ, Yoon SH, Mochida I. The bimetallic effects of catalysts on the syntheses of thin carbon nanofibers. *J Phys Chem C*. 2008;112:10050–10060.
31. See CH, Dunens OM, MacKenzie KJ, Harris AT. Process parameter interaction effects during carbon nanotube synthesis in fluidized beds. *Ind Eng Chem Res*. 2008;47:7686–7692.
32. Naghash AR, Xu Z, Etsell TH. Coprecipitation of nickel-copper-aluminum takovite as catalyst precursors for simultaneous production of carbon nanofibers and hydrogen. *Chem Mater*. 2005;17:815–821.
33. Shaijumon MM, Bejoy N, Ramaprabhu S. Catalytic growth of carbon nanotubes over Ni/Cr hydrotalcite-type anionic clay and their hydrogen storage properties. *Appl Surf Sci*. 2005;242:192–198.
34. Yu Z, Chen D, Rønning M, Vrålstad T, Ochoa-Fernández E, Holmen A. Large-scale synthesis of carbon nanofibers on Ni-Fe-Al hydrotalcite derived catalysts I. Preparation and characterization of the Ni-Fe-Al hydrotalcites and their derived catalysts. *Appl Catal A*. 2008;338:136–146.
35. Yu Z, Chen D, Rønning M, Tøtdal B, Vrålstad T, Ochoa-Fernández E, Holmen A. Large-scale synthesis of carbon nanofibers on Ni-Fe-Al hydrotalcite derived catalysts II: effect of Ni/Fe composition on CNF synthesis from ethylene and carbon monoxide. *Appl Catal A*. 2008;338:147–158.
36. Dussault L, Dupin JC, Guimon C, Monthioux M, Latorre N, Ubieto T, Romeo E, Royo C, Monzón A. Development of Ni-Cu-Mg-Al catalysts for the synthesis of carbon nanofibers by catalytic decomposition of methane. *J Catal*. 2007;251:223–232.
37. Zhao Y, Jiao Q, Li C, Liang J. Catalytic synthesis of carbon nanostructures using layered double hydroxides as catalyst precursors. *Carbon*. 2007;45:2159–2163.
38. Benito P, Herrero M, Labajos FM, Rives V, Royo C, Latorre N, Monzon A. Production of carbon nanotubes from methane: use of

Co-Zn-Al catalysts prepared by microwave-assisted synthesis. *Chem Eng J*. 2009;149:455–462.
39. Li F, Tan Q, Evans DG, Duan X. Synthesis of carbon nanotubes using a novel catalyst derived from hydrotalcite-like Co-Al layered double hydroxide precursor. *Catal Lett*. 2005;99:151–156.
40. Xiang X, Zhang L, Hima HI, Li F, Evans DG. Co-based catalysts from Co/Fe/Al layered double hydroxides for preparation of carbon nanotubes. *Appl Clay Sci*. 2009;42:405–409.
41. Xiang X, Hima HI, Wang H, Li F. Facile synthesis and catalytic properties of nickel-based mixed-metal oxides with mesopore networks from a novel hybrid composite precursor. *Chem Mater*. 2008;20:1173–1182.
42. Wang Q, Li H, Chen L, Huang X. Monodispersed hard carbon spherules with uniform nanopores. *Carbon*. 2001;39:2211–2214.
43. Ogawa M, Kaido H. Homogeneous precipitation of uniform hydrotalcite particles. *Langmuir*. 2002;18:4240–4242.
44. Sun X, Li Y. Colloidal Carbon spheres and their core/shell structures with noble-metal nanoparticles. *Angew Chem Int Ed Engl*. 2004;43:597–601.
45. Li F, Duan X. Applications of layered double hydroxides. *Struct Bonding*. 2006;119:193–223.
46. Inagaki M. *New Carbons: Control of Structure and Functions*. Amsterdam: Elsevier, 2000.
47. Mathur RB, Seth S, Lal C, Rao R, Singh BP, Dhami TL, Rao AM. Cosynthesis, purification and characterization of single- and multi-walled carbon nanotubes using the electric arc method. *Carbon*. 2007;45:132–140.
48. Ago H, Kugler T, Cacialli F, Salaneck WR, Shaffer MSP, Windle AH, Friend RH. Work functions and surface functional groups of multiwall carbon nanotubes. *J Phys Chem B*. 1999;103:8116–8121.
49. Tessonnier JP, Rosenthal D, Hansen TW, Hess C, Schuster ME, Blume R, Girgsdies F, Pfänder N, Timpe O, Su DS, Schlögl R. Analysis of the structure and chemical properties of some commercial carbon nanostructures. *Carbon*. 2009;47:1779–1798.
50. Zhang G, Sun S, Yang D, Dodelet JP, Sacher E. The surface analytical characterization of carbon fibers functionalized by H_2SO_4/HNO_3 treatment. *Carbon*. 2008;46:196–205.
51. Reich S, Thomsen C, Maultzsch J. *Carbon Nanotubes: Basic Concepts and Physical Properties*. Weinheim, Germany: Wiley, 2004.
52. Dresselhaus MS, Dresselhaus G, Saito R, Jorio A. Raman spectroscopy of carbon nanotubes. *Phys Rep*. 2005;409:47–99.

Manuscript received Aug. 14, 2009, and final revision received Jan. 13, 2010.